Mechanochemical Synthesis of Methylammonium Lead Mixed–Halide Perovskites: Unraveling the Solid-Solution Behavior using Solid-State NMR

*Abhoy Karmakar,[1§] Abdelrahman M. Askar,[2§] Guy M. Bernard,[1] Victor V. Terskikh,[3] Michelle Ha,[1] Sahil Patel,[2] Karthik Shankar,[2,4] and Vladimir K. Michaelis[1]**

1-Department of Chemistry, University of Alberta, Edmonton, Alberta, Canada, T6G 2G2

2-Department of Electrical and Computer Engineering, University of Alberta, Edmonton, Alberta, Canada, T6G 1H9

3-Department of Chemistry, University of Ottawa, Ottawa, Ontario, Canada, K1N 6N5

4-NRC National Institute for Nanotechnology, Edmonton, Alberta, Canada, T6G 2M9

[§] co-authors contributed equally

[*]Corresponding author: vladimir.michaelis@ualberta.ca

ABSTRACT

Mixed halide lead perovskite (MHP) materials are rapidly advancing as next-generation high-efficiency perovskite solar cells due to enhanced stability and bandgap tunability. In this work, we demonstrate the ability to readily and stoichiometrically tune the halide composition in methylammonium-based MHPs using a mechanochemical synthesis approach. Using this solvent-free protocol we are able to prepare domain-free MHP solid solutions with randomly distributed halide ions about the Pb center. Up to seven distinct $[PbCl_xBr_{6-x}]^{4-}$ environments are identified, based on the ^{207}Pb NMR chemical shifts, which are also sensitive to the changes in the unit cell dimensions resulting from the substitution of Br by Cl, obeying Vegard's law. We demonstrate a straightforward and rapid synthetic approach to forming highly tunable stoichiometric MHP solid solutions while avoiding the traditional solution synthesis method by redirecting the thermodynamically driven compositions. Moreover, we illustrate the importance of complementary characterization methods, obtaining atomic-scale structural information from multinuclear, multifield and multidimensional solid-state magnetic resonance spectroscopy, as well as from quantum chemical calculations, and long-range structural details using powder X-ray diffraction. The solvent-free mechanochemical synthesis approach is also compared to traditional solvent synthesis, revealing identical solid-solution behavior; however, the mechanochemical approach offers superior control over the stoichiometry of the final mixed halide composition, which is essential for device engineering.

INTRODUCTION

Hybrid organic-inorganic metal halide perovskites have emerged as promising contenders for next-generation low-cost, high-efficiency solar cells. Fueled by intensive worldwide research efforts, perovskite solar cells (PSCs) surpassed the 22% photoconversion efficiency limit within the first few years.[1] This rapid improvement in PSC efficiencies is due to their promising intrinsic properties such as long-range ambipolar carrier diffusion lengths, high absorption coefficients, and low exciton binding energies.[2-4] A particularly promising area of research has been on mixed halide perovskites (MHPs) of the type ABX_3, where A = $CH_3NH_3^+$, B = Pb^{2+} and X = Cl^-, Br^-, I^-.[5] One advantage MHPs offer is the bandgap tunability made possible through the halide composition, which is important for applications such as tandem solar cells and light emitting diodes (LEDs).[6] Additionally, MHPs offer enhanced stability against moisture and thus their use to achieve more stable and higher-performing PSCs is becoming routine.[7, 8]

MHPs possess an intriguing range of properties stemming from the degrees of freedom in their synthesis due to the relatively easy reversible-halide exchange both in solution and between gas and solid phases.[9, 10] Nevertheless, challenges with MHPs have also been reported. In particular, the consequences of halide ion mobility on the device performance[11-13] and of phase segregation due to photo-induced halide ion migration[14-17] must be considered. Amongst the many synthesis techniques for preparing perovskite materials, mechanochemical synthesis (MCS) has gained renewed interest due to the advantages it offers. MCS is a straightforward, green-chemistry method which is highly efficient, simple, and reproducible. Moreover, it is a solvent-free method that also avoids high-temperature reactions and is capable of mass-yield production. MCS has previously been applied in other systems,[18-21] but recently has shown

promise in the preparation of bulk and nanocrystalline perovskites,[22-26] achieving enhanced material properties and device performance[27, 28] compared to those prepared using traditional solvent synthesis (SS). For instance, preparing $CH_3NH_3PbI_3$ PSCs by MCS leads to a reduction in the interfacial trap density in fabricated PSCs in comparison to the same compound prepared through standard solvent synthesis.[29] Recently, MCS was used to prepare complex mixed cation (Cs, Rb, formamidinium, in addition to methylammonium) lead halide perovskite materials used in the highest performing and most stable PSCs reported to date, revealing similar structural properties to the corresponding perovskite materials prepared by traditional two-step casting techniques.[30]

The high mobility of halide ions in halide perovskites prompted us to investigate the potential of MCS in the synthesis of $MAPb(X_xX'_{1-x})_3$ (MA = $CH_3NH_3^+$, X and X' = Cl^- and Br^- or Br^- and I^-) MHPs for the first time from their parent $MAPbX_3$ compounds and to examine at the atomic scale the true halide mixing in the products. A suite of techniques, including solid-state nuclear magnetic resonance (NMR) spectroscopy, a powerful tool in probing the local- and medium-range chemical environments of NMR-active nuclides, were used in our investigation. Specifically, in this work ^{207}Pb NMR spectroscopy was used to investigate the change in the Pb chemical environment of these MHPs, complemented by X-ray diffraction (XRD) data and quantum chemical calculations. The challenge is to synthesize stoichiometric and homogenous mixed-halide variants, avoiding microscopic domains or inhomogeneous phase-separated solid mixtures. X-ray diffraction approaches are excellent for the determination of the long-range crystalline structure while NMR spectroscopy is one of the few characterization tools capable of measuring atomic-level structure, providing direct information regarding the local chemical environment that is impacted by ion substitutions or rearrangements such as defect sites, solid

solutions or segregated domains within solids.[31-34] For example, it has been suggested that Cl and Br can substitute for one another in $MAPbX_3$, forming a crystalline perovskite with different domains when synthesized using the traditional solvent synthesis as well as high-temperature solid-state synthesis approaches.[35]

In this report, we demonstrate two mechanochemical stoichiometric synthetic approaches that produce polycrystalline single-phase, ordered or locally disordered MHP solid-solutions with random halide arrangements about the Pb center, avoiding phase-segregated domains. The techniques used for the application of MCS (Scheme 1) were manual hand grinding (HG) using a mortar and pestle and a ball milling (BM) method. When appropriate, our MCS results are compared to those obtained from samples prepared by traditional SS protocols.[35] $MAPbI_3$ prepared using the MCS method has been shown to yield a product with superior solar cell performance compared to the corresponding product prepared via SS;[29] thus, we demonstrate that the MCS route described herein for the more commonly used MHPs is a very promising technique as an efficient strategy for commercializing these systems for a wide variety of photovoltaic and optoelectronic applications.

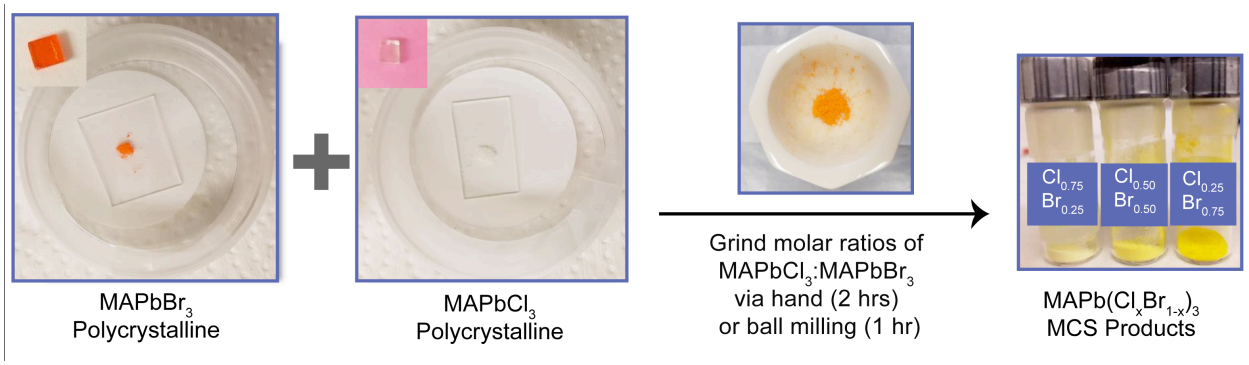

Scheme 1: MCS process for the preparation of MHPs. In the HG method, parent compounds are mixed in the required molar ratio using a mortar and pestle and the HG process continues for 1-2 hrs to obtain a uniform single-phase product. In MCS-BM, a similar approach is used, but instead of the HG process, an automated BM system is used for 1 hr.

EXPERIMENTAL

All starting precursor materials and solvents were obtained from commercial sources, and used without further purification: lead(II) iodide (99%), lead(II) bromide (+98%) and lead(II) chloride (99%) from ACROS Organics (Morris Plains, NJ, USA), methylammonium chloride, γ-butyrolactone (GBL) (> 99 %) and dimethyl sulfoxide (DMSO) from Sigma Aldrich (St. Louis, MO, USA) and methylammonium bromide (MABr) and methylammonium iodide (MAI) from Dyesol LTD (Australia).

Synthesis of $MAPbX_3$ using the Inverse Temperature Crystallization (ITC) Technique:[36, 37]

$MAPbCl_3$: A 1 M $MAPbCl_3$ solution was prepared by adding MACl and $PbCl_2$ in a 1:1 V/V DMF:DMSO mixture at room temperature. A clear transparent solution formed, which was filtered with 0.2 μm filters. The solution was then distributed into small vials, with 2 ml solution each. These vials were placed in an oil bath at 60 ˚C and the large crystals were allowed to grow for 6 hours, then washed thoroughly with DMF and immediately dried with a N_2 gas flow.

$MAPbBr_3$: A 1 M $MAPbBr_3$ solution was prepared at room temperature by adding MABr and $PbBr_2$ in dimethylformamide (DMF). The resulting mixture formed a clear transparent solution. The solution was filtered using 0.2 μm filters, then distributed into small vials with 2 ml of solution each. The vials were placed in an oil bath at 80 ˚C and the large crystals were allowed to grow for 3 hours then washed thoroughly with DMF and immediately dried with a dry N_2 gas flow.

$MAPbI_3$: A 1 M $MAPbI_3$ solution was prepared by fully dissolving MAI and PbI_2 in GBL at 60 ˚C such that it became a bright yellow solution. The solution was filtered using 0.2 μm filters, then distributed into small vials with 2 ml of solution each. The vials were placed in an oil bath

at 110 ˚C. The large crystals were allowed to grow for 3 hours, then washed thoroughly with GBL and immediately dried with an N_2 gas flow, then stored under vacuum in the dark.

Synthesis of $MAPbX_xX'_{3-x}$ MHPs:

To synthesize MHPs using the MCS-HG approach, $MAPbX_3$ and $MAPbX'_3$ were loaded with molar ratios set to achieve the desired mixed halide composition. For example, to prepare $MAPb(Cl_{0.5}Br_{0.5})_3$, 159.66 mg of $MAPbBr_3$ was loaded in a mortar with 115.21 mg of $MAPbCl_3$ and hand grinding was applied for 1-2 hrs. For MCS-BM techniques, the same ratios of precursors as for the MCS-HG approach were loaded into either a planetary (RETSCH Planetary Ball Mill PM 100) or shaker ball mill (SPEX^{TM} SamplePrep 8000 Mixer/Mill). We note that by adjusting the time, ball size and speed of impacts, one can utilize a planetary mill to obtain similar results to HG within a fraction of the time (i.e., 5 - 60 minutes) with good reproducibility. All synthetic procedures were carried out under ambient lab conditions in air. All results presented here for the MCS-BM method were obtained from parent compounds processed by the shaker ball mill for 1 hr.

Diffuse Reflectance (DR) Spectroscopy of MHP Perovskites:

A Varian Cary 400 UV-Visible spectrophotometer, equipped for the analysis of small quantity fine powdered samples, was used to obtain DR data. Each sample was packed into a black boat (loaded with ~100 mg/sample), with each measurement acquired between wavelengths of 300 and 900 nm.

Powder X-Ray Diffraction (XRD) Measurements:

Fine powder samples were mounted on a glass slide and analyzed using a Bruker D8 Advance Diffractometer equipped with a Cu-K_α source and a VANTEC-500 2D detector. All data were acquired at room temperature with a 2θ range of 10° - 60° and 0.02° resolution.

Solid-state Nuclear Magnetic Resonance (NMR) Spectroscopy:

^{1}H NMR spectra were acquired at 7.05 T (^{1}H, 300.4 MHz) on a Bruker Avance 300 NMR spectrometer with a Bloch pulse using a 4.0 μs π/2 pulse ($\gamma B_1/2\pi$ = 62.5 kHz) and a recycle delay of 60 s. Samples were packed in 4 mm OD ZrO_2 rotors and spectra were acquired with a magic-angle spinning (MAS) frequency of 10 kHz. All ^{1}H spectra were referenced to TMS (δ (^{1}H) = 0.0 ppm) by setting the ^{1}H peak of adamantane to 1.85 ppm.

^{13}C NMR spectra were acquired at 7.05 T on a Bruker Avance 300 NMR spectrometer equipped with a 4 mm double resonance MAS NMR probe. ^{13}C (ν_L = 75.5 MHz) cross-polarization (CP)[38] MAS NMR spectra were acquired with a spinning frequency of 10 kHz, a 4.0 μs π/2 pulse ($\gamma B_1/2\pi$ = 62.5 kHz) for ^{1}H, a contact time of 3.5 ms, and a recycle delay time of 60 s. All ^{13}C spectra were referenced to TMS (δ(^{13}C) = 0.0 ppm) by setting the high frequency ^{13}C peak of solid adamantane to 38.56 ppm.[39] All spectra were acquired with TPPM high-power ^{1}H decoupling ($\gamma B_1/2\pi$ = 62.5 kHz).[40]

^{207}Pb NMR spectra were acquired at 7.05, 11.7 and 21.1 T on Bruker Avance 300, 500 and Avance II 900 NMR spectrometers, respectively. Non-spinning ^{207}Pb NMR spectra were collected using a 4 mm double resonance H/X Bruker probe, using either a Hahn-echo[41] ($(\pi/2)_x$-τ_1-$(\pi)_y$-τ_2-ACQ where τ represents the inter-pulse (τ_1) and refocusing delays (τ_2)) or a modified quadrupolar-echo[42-44] pulse sequence to achieve broader excitation width and minimize line distortions at higher magnetic field strengths. A recycle delay of 5.0 s, a 4.0 μs π/2 pulse ($\gamma B_1/2\pi$ = 62.5 kHz) and τ_1 values of 20 - 30 μs were used for all the measurements to minimize the impact of echo delay on the quantitative assessment of peak areas. T_2 values were measured using a spin-echo pulse sequence and are summarized in Supporting Information. At 11.7 and 21.1 T, the variable offset cumulative spectra (VOCS)[45] approach using between 3 and 5

steps with a 50 kHz transmitter stepping frequency across the spectral range was used to ensure acquisition of the complete, undistorted spectrum; the sub-spectra were added using the skyline projection method. Two-dimensional ^{207}Pb EXSY (EXchange SpectroscopY)[46] spectra (21.1 T) were acquired using a series of mixing times between 10 μs and 2 ms. A total of 64 to 128 slices were collected in the indirect dimension using a 2 μs increment and between 512 to 3,840 co-added transients were acquired per slice, depending on mixing time. All ^{207}Pb NMR spectra were referenced to $PbMe_4$ ($\delta(^{207}Pb)$ = 0.0 ppm) by setting the ^{207}Pb peak of non-spinning solid $MAPbCl_3$ measured at 293 K to –647.5 ppm.[47]

NMR Processing, Fitting Procedures and NMR Considerations:

Spectra were processed using Topspin 3.5 Bruker software with between 250 and 500 Hz exponential apodization and the data were fit using both OriginPro 8 and WSOLIDS[48] software. To assess the quantitative nature of the unique $[PbX_xX'_{6-x}]^{4-}$ chemical environments observed in the ^{207}Pb NMR spectra, all data were fit using two distinct fitting procedures to assess the distributions of sites. Within Origin, all data were fit using Gaussian lineshapes and up to seven distinct Pb environments. Spectra were also fit using WSOLIDS, with seven distinct Pb environments to incorporate the anisotropic components as surmised from spectra acquired at multiple magnetic fields and from the results of density functional theory (DFT) calculations. See Supporting Information (SI) for a more thorough explanation of the fitting procedure including errors and statistical analysis. To ensure maximum resolution, these samples were initially assessed using a combination of multiple magnetic field strengths (i.e., 7.05, 11.75 and 21.1 T), non-spinning and magic-angle spinning (MAS) NMR methods and experiments with and without ^{1}H decoupling. The benefit of MAS is minimal (see Supporting Information, Table S1) removing a small effect from heteronuclear dipole couplings between Pb and X;[47, 49-53] while

high-power proton decoupling did not significantly affect the overall lineshape or width compared to those obtained without ^{1}H decoupling; this is attributed to the fast motion of the MA cation that rotates rapidly within the cuboctahedron and therefore its ^{1}H nuclei self-decouple from the Pb. Chemical shift anisotropy was detectable under certain conditions with low mixed halide doping, using a combination of MAS and non-spinning experiments (see below and SI). Overall, site resolution increased at higher magnetic field strengths. To gauge the effect of using an echo pulse sequence to quantify Pb chemical environments, a series of spectra were acquired with varying τ values (10 - 50 μs); the relative intensities across all sites (MCS-HG; $MAPb(Cl_{0.5}Br_{0.5})_3$) were nearly identical (< 2%), ensuring a robust approach. MAS spectra were routinely avoided to limit the impact of unwanted frictional heating on the ^{207}Pb chemical shifts, which are known to be extremely sensitive to temperature.[47] Hence, most ^{207}Pb NMR spectra were acquired under non-spinning conditions without ^{1}H decoupling.

Quantum Chemical Calculations:

Relativistic calculations on model $[PbCl_xBr_{6-x}]^{4-}$ anions: Density functional theory (DFT) calculations of the Pb magnetic shielding on a series of 10 $[PbCl_xBr_{6-x}]^{4-}$ octahedral model anions were carried out using the Amsterdam Density Functional (ADF) 2017 modeling suite.[54-57] The structures were modeled by assuming octahedral coordination about the Pb, with a Pb-Cl bond length of 2.834 Å, derived from XRD data (vide infra), and a Pb-Br bond length of 2.966 Å.[57] A calculation for $[PbI_6]^{4-}$ also assumed octahedral symmetry and a bond length of 3.146 Å.[57] Relativistic effects were calculated using the zeroth order regular approximation (ZORA) method along with the ZORA/QZ4P basis set, which is optimized for relativistic calculations.[58, 59] All calculated shielding values were converted to chemical shifts using δ_{calc} (ppm) = $-(\sigma_{calc.} - 8858.4$ ppm); the relationship was determined from a linear regression between experimental

chemical shifts and the calculated magnetic shielding values of the three parent compounds $MAPbCl_3$, $MAPbBr_3$ and $MAPbI_3$. All principal components of the calculated ^{207}Pb magnetic shielding tensors are available in the supporting information and are defined using the Maryland Convention.[60, 61] All DFT calculations used the Perdew, Burke, and Ernzerhof (PBE) functional in the generalized gradient approximation (GGA).[62-64]

Periodic calculations: Gauge including projector augmented wave (GIPAW) based DFT calculations, a plane-wave basis set ideal for computing properties in periodic systems,[65] were undertaken on model 2 × 2 × 2 super-cells with primitive symmetry, as implemented in the CASTEP program (ver. 4.4). In these calculations, ^{207}Pb magnetic shielding values were obtained on a series generated by systematically replacing Cl for Br in $MAPbCl_3$. The calculations used the PBE functional in the GGA for the exchange-correlation energy[62, 63] and ultrasoft pseudopotentials.[66] All calculations were performed on an HP xw4400 workstation with a single Intel Dual-Core 2.67 GHz processor and 8 GB RAM. No further optimizations were performed regarding the unit cell. An all-atom geometry optimization was performed on the 50:50 *fac*- and *mer*- isomers; however, these did not provide significant changes to the calculated magnetic shielding parameters and all forces on heavier atoms were below the 0.48 eV/Å threshold and thus no further optimization within the computed structures were performed. All calculations were performed with a coarse accuracy basis set and a maximum plane-wave energy of 250.34 eV.

RESULTS AND DISCUSSION

Figure 1 shows ^{207}Pb NMR spectra of $MAPb(Cl_{0.5}Br_{0.5})_3$ prepared using the MCS-BM (Figure 1a), MCS-HG (Figure 1b) and SS (Figure 1c) approaches, acquired at magnetic field strengths ranging from 7.05 to 21.1 T. The ^{207}Pb NMR spectra exhibit multiple sites, regardless of synthetic approach, illustrating the complex short-range Pb structure present in these otherwise simple primitive cubic crystalline solids (*Pm*-3*m* space group).[67] The resolution achieved at higher magnetic field strengths suggests distinct local Pb chemical environments with a potential to assign the various arrangements of halide ions within the MHPs qualitatively and quantitatively. This initial finding suggests that each $[PbX_xX'_{6-x}]^{4-}$ unit bears distinct NMR chemical shifts for the various Pb-halide octahedral arrangements demonstrating a binomial-like distribution characteristic of solid solution random halide mixing behavior.

To date, most of the hybrid perovskite studies have relied extensively on diffraction-based approaches.[68, 69] Solid-state NMR spectroscopy, however, is rapidly emerging as an extremely informative analytical structural tool in characterizing both local structure and dynamics within photovoltaic perovskite materials.[30, 35, 47, 49, 51, 70-74] In particular, ^{207}Pb is an information-rich, receptive spin-1/2 nucleus that exhibits a very large chemical shift range and thus is sensitive to even minor changes in local chemical environment. However, unlike solution NMR spectroscopy, solid-state NMR spectra are often subject to broad lines typically arising from various anisotropic interactions. For lead halide perovskites, these can include unfavorable T_2 characteristics, small heteronuclear dipolar coupling contributions (< 1 kHz), ^{207}Pb-$^{35/37}$Cl, ^{207}Pb-$^{79/81}$Br or ^{207}Pb-^{127}I indirect spin-spin (*J*-coupling) interactions, and the potential of magnetic shielding anisotropy when the nucleus is not at a center of cubic symmetry.[35, 47, 49-51, 70, 72] For the

work presented here, line broadening may also result from the presence of isomers such as *cis* and *trans* $[PbX_4X'_2]^{4-}$ and *fac* and *mer* isomers in the $[PbX_3X'_3]^{4-}$ mixed halide octahedron environments, or from localized disorder within the lead octahedra similar to the effects often seen in lead-containing glasses.[75, 76] Therefore, the chemical shifts of the peak maxima, δ_{cs}, are reported below instead of conventional isotropic chemical shift, δ_{iso} since at lower magnetic field strengths *J*-based splitting[72] may become apparent or at higher magnetic fields (e.g., 35 T) magnetic shielding anisotropy[77] may begin to dominate the spectrum. The observed ^{207}Pb NMR results (i.e., broad peaks, chemical shift distributions) for the BM, SS and HG samples discussed above warranted further investigation to assess and interpret the local atomic structure.

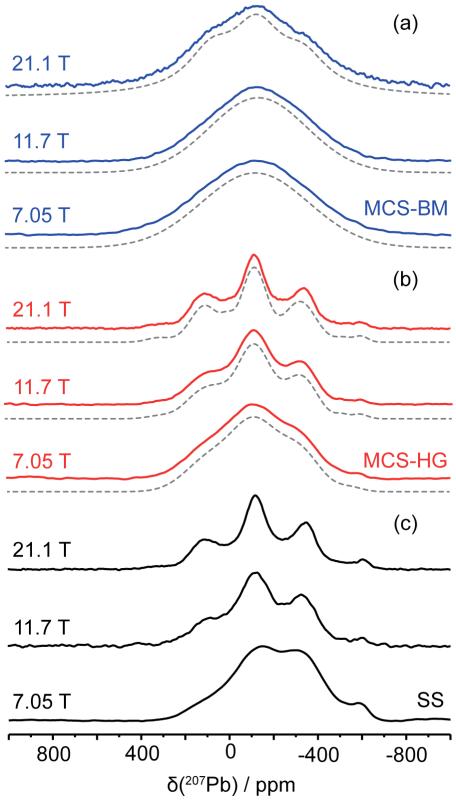

Figure 1: ^{207}Pb NMR spectra of non-spinning MCS-BM (a, blue), MCS-HG (b, red) and SS (c, black) samples of $MAPb(Cl_{0.5}Br_{0.5})_3$, acquired at 7.05 T (300 MHz, ^{1}H), 11.7 T (500 MHz, ^{1}H) and 21.1 T (900 MHz, ^{1}H). The grey dotted lines are the best fits for the spectra obtained for the samples prepared with the mechanochemical synthesis methods.

MAPb(Cl_xBr_{1-x})$_3$ Hand Ground Mechanochemical Synthesis

To unravel the complex nature of anion mixing about the Pb center of the MHPs prepared with the SS and MCS methods, a series of standards of various $MAPbCl_3$/$MAPbBr_3$ molar ratios (100/0, 95/5, 83/17, 75/25, 50/50, 25/75, 5/95 and 0/100) were synthesized using the inverse temperature crystallization (parent compounds)[36, 37] and MCS-HG (MHPs) methods and analyzed by ^{207}Pb NMR spectroscopy to assess the changes in the first coordination sphere about the Pb.

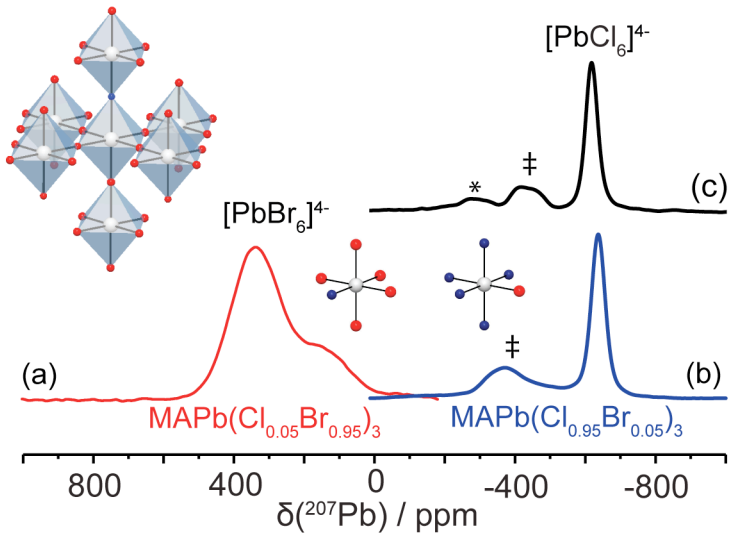

Figure 2: ^{207}Pb NMR spectra (B_o = 11.7 T) of (a) non-spinning $MAPb(Cl_{0.05}Br_{0.95})_3$ prepared by MCS-HG, (b) non-spinning and (c) MAS ($\omega_r/2\pi$ = 13.5 kHz) NMR spectra of $MAPb(Cl_{0.95}Br_{0.05})_3$ prepared by MCS-HG. The δ_{cs} are marked with ‡ and the spinning sideband is identified by an asterisk (*).

Figure 2a shows a non-spinning ^{207}Pb NMR spectrum for $MAPb(Cl_{0.05}Br_{0.95})_3$, with two peaks located at $\delta_{cs} \approx 340$ and 175 ppm. The pattern seen in Figure 2a is similar to that expected for a single NMR site experiencing chemical shift anisotropy (CSA). To investigate, an MAS spectrum of the sample was obtained at 7.1 T at a spinning frequency of 13 kHz. The spectrum, which is slightly asymmetric, can best be simulated with two NMR sites separated by approximately 135 ppm or 8.5 kHz (i.e., less than the spinning frequency and hence a second NMR site rather than a spinning sideband) and with the expected intensity of approximately 30

% for the low frequency site (see Figure S1). This result is corroborated by DFT calculations (Table S2), which predict that $[PbBr_5Cl_1]^{4-}$ appears at approximately 50 ppm to lower chemical shift from the peak for $[PbBr_6]^{4-}$. Likewise, the ^{207}Pb NMR spectrum for $MAPb(Cl_{0.95}Br_{0.05})_3$ (Figure 2b) also contains two peaks, at $\delta_{cs} \approx -641$ and -400 ppm; the corresponding MAS spectrum for the latter (Figure 2c) yield similar values, $\delta_{iso}^{MAS} \approx -621$ and -450 ppm. The peak at -450 ppm, attributed to $[PbCl_5Br_1]^{4-}$ units, appears to be a doublet. However, close examination reveals that the peak is asymmetric, appearing skewed towards its high-frequency edge (see Figure S2 for an expansion of this region and for a comparison with a spectrum obtained at 7.05 T). As seen from this expansion, the peaks do not represent two distinct NMR sites, since in such a case the chemical shifts of these peaks would be the same regardless of magnetic field strength. A ^{207}Pb nucleus within a $[PbCl_5Br_1]^{4-}$ unit under MAS conditions is subject to $^1J(^{207}Pb,^{35/37}Cl)$ interactions to the five Cl nuclei and a $^1J(^{207}Pb,^{79/81}Br)$ interaction to the Br, but the latter is expected to dominate.[72] However, the large nuclear quadrupolar coupling expected for $^{79/81}$Br (NQR frequencies of 70.451 and 58.842 MHz have been reported for $MAPbBr_3$)[78] will result in an asymmetric splitting pattern[79] rather than the four equal intensity peaks one may expect in the absence of a large quadrupole interaction. The presence of a spinning sideband for the NMR site at -450 ppm is consistent with the asymmetry of the $[PbCl_5Br_1]^{4-}$ unit and the fact that it is shifted to higher frequency by approximately 170 ppm is qualitatively in agreement with the trend predicted by DFT calculations (vide infra).

At dopant level halide substitutions (i.e., $\leq 5\%$), the halide ion transitions into the lattice replacing a Br for Cl (or Cl for Br) and immediately affects the lattice parameters (vide infra) of the solid-solution and the corresponding $\delta_{cs}(^{207}Pb)$ chemical shifts of $[PbBr_6]^{4-}$ or $[PbCl_6]^{4-}$, reflecting the sensitivity of ^{207}Pb NMR spectroscopy to changes within the material. Thus, it is

not surprising that the chemical shift of a slightly Br-doped material is greater than that for the pure parent material ($MAPbCl_3$) since the ^{207}Pb resonance of the $MAPbBr_3$ parent complex appears at a higher chemical shift. Accounting for the 5% dopant concentration and for the coordination number of Pb (i.e., 6), 26.5% of the Pb centers are directly coordinated to a Br (or Cl) dopant within their octahedra. Fitting the peak areas for the ^{207}Pb NMR spectra for $MAPb(Cl_{0.05}Br_{0.95})_3$ and for $MAPb(Cl_{0.95}Br_{0.05})_3$, respectively, yielded ratios of 0.72:0.28 (± 0.05) and 0.28:0.72 (±0.02) for the $[PbBr_6]^{4-}$ and $[PbCl_1Br_5]^{4-}$ units of the former and for the $[PbCl_5Br_1]^{4-}$ and $[PbCl_6]^{4-}$ units of the latter. Therefore, the lower-frequency resonance in the ^{207}Pb NMR spectrum for $MAPb(Cl_{0.05}Br_{0.95})_3$ is assigned to a $[PbClBr_5]^{4-}$ local six-coordinate environment; likewise, the higher-frequency resonance observed in $MAPb(Cl_{0.95}Br_{0.05})_3$ is assigned to $[PbCl_5Br_1]^{4-}$. A small CSA contribution (span, $\Omega = \delta_{11} - \delta_{33} \approx 200 \pm 30$ ppm) was determined for the $MAPb(Cl_{0.95}Br_{0.05})_3$ by using a combination of MAS and non-spinning experiments at 11.7 T; this was only possible for this sample due to the narrow resonance of the $[PbCl_6]^{4-}$ octahedra (Figure 2c). Using this finding and the DFT results (vide infra) we expect only a minor CSA contribution from the $[PbClBr_5]^{4-}$ ^{207}Pb environment found in the $MAPb(Cl_{0.05}Br_{0.95})_3$ sample; unfortunately the breadth of these two sites and the lack of resolution between them limits our ability to isolate potential anisotropic shielding, dipolar and *J*-coupling contributions or to accurately investigate spin-lattice or spin-spin relaxation mechanisms.

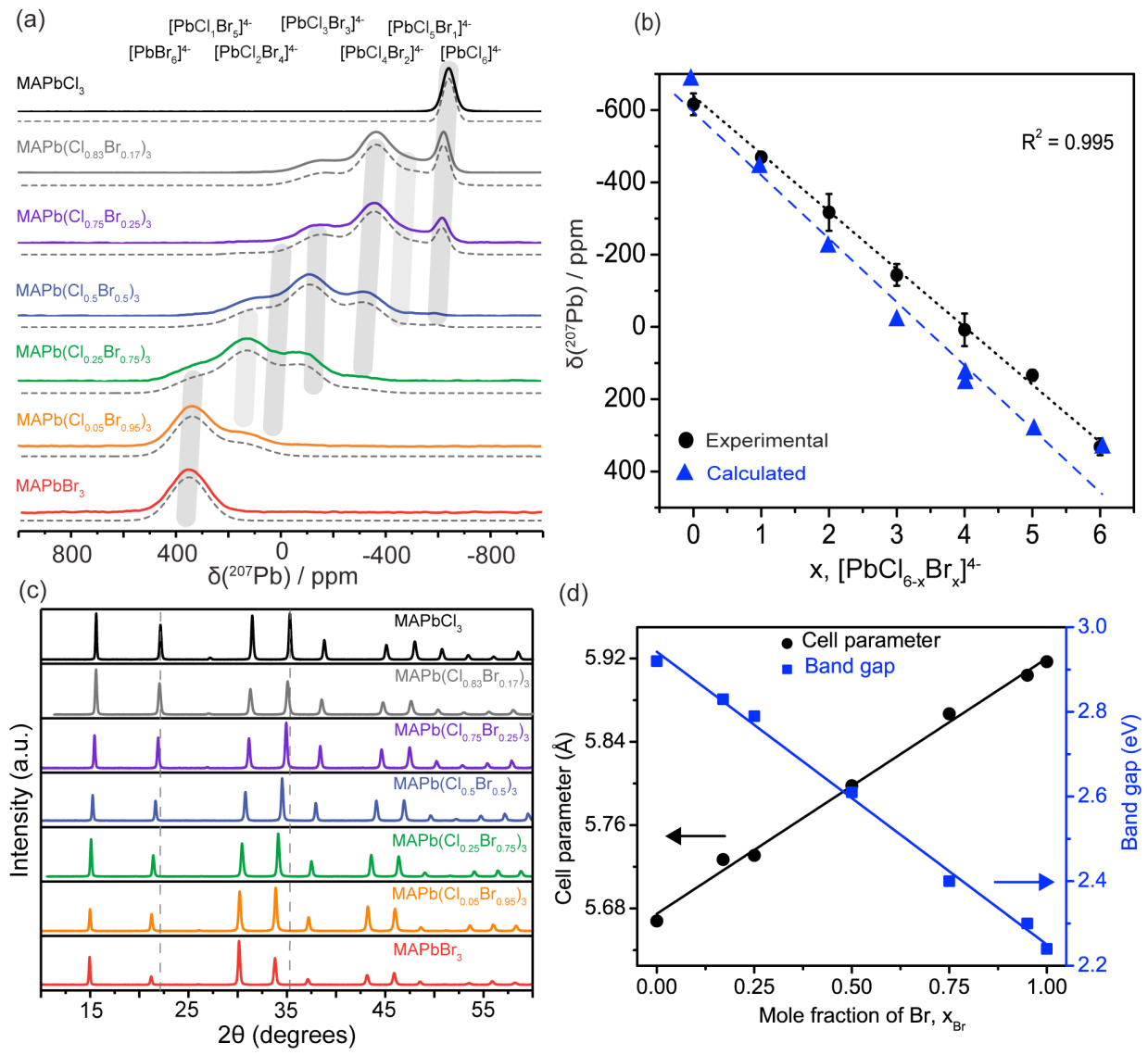

Figure 3: Non-spinning ^{207}Pb NMR spectra (11.7 T) of MCS-HG MHPs and their parent compounds (a); the assignment of the NMR peaks is shown at the top (the shaded areas are guides to the eye to identify specific NMR sites in the various spectra, and the dashed lines indicate simulated spectra). See the Supporting Information for an explanation of how these spectra were fit. Linear relationship of $\delta(^{207}\text{Pb})$ with substitution of Cl with Br (experimental, circles and $\delta_{iso}(^{207}\text{Pb})$ quantum chemical calculations (ADF), triangle), (b). Powder X-ray diffraction data (c), dotted lines are guides to the eye, and a plot of cell parameter (R^2 = 0.994) and experimentally determined bandgaps extracted from Tauc plots (R^2 = 0.994) vs Br mole fraction for the MHP series (d).

As Cl replaces Br, the ^{207}Pb spectra break into additional resonances due to the formation of new Pb-X bonds whereby peak maxima shift to lower chemical shifts towards that for the parent

compound, $MAPbCl_3$ (Figure 3a). These spectra demonstrate the sensitivity of ^{207}Pb NMR spectroscopy, as exemplified by the extremely large chemical shift range (~17,000 ppm) for this nucleus,[80] to the halide environment about the Pb center in these samples.[52, 81] See Figure S3 and the accompanying section in Supporting Information for a discussion of how the spectra for the MHPs illustrated above were de-convoluted. A clear, although smaller, increase in the chemical shift is also observed for the resonance attributed to $[PbCl_6]^{4-}$ with increasing Br content, as shown in Table 1; this is attributed to the change in the unit cell parameters as it expands to allow Br incorporation (Figure S4). Table 1 summarizes the distinct ^{207}Pb δ_{cs} values for each $[PbCl_xBr_{6-x}]^{4-}$ (x = 0 to 6) octahedron. Using these data, we determined a linear correlation between $\delta_{cs}(^{207}Pb)$ and the hexa-substituted Pb-X chemical environments (Figure 3b) that can be used to identify the distinct $[PbCl_xBr_{6-x}]^{4-}$ environments according to $\delta_{cs}(^{207}Pb/ppm) = 160\square M - 640$, where M is the number of Br atoms in the first coordination sphere of Pb. Moreover, a similar linear relation exists between the electronegativity of the mixed halide ions and the chemical shift in ^{207}Pb NMR spectra for each of the corresponding $[PbCl_xBr_{6-x}]^{4-}$ environments (Figure S5). The ^{207}Pb NMR linewidths for $MAPbX_3$ increase as X is substituted from Cl to Br to I (Table S1), and thus the ^{207}Pb resonance for a site with more Br neighbors is expected to be broader than that for a site with more Cl neighbors, and likewise when I is substituted for Br.[47, 49, 70] The ^{207}Pb spin-spin relaxation times (T_2) for the individual $[PbX_xX'_{6-x}]^{4-}$ chemical environments present in the MCS-HG $MAPb(Cl_{0.5}Br_{0.5})_3$ sample range from 54 μs for $[PbBr_6]^{4-}$ to 98 μs for $[PbCl_6]^{4-}$, with a small systematic increase in T_2 as Cl replaces Br about the Pb center (Table S3). Previous studies on the parent materials indicate the T_2 values to be nearly an order of magnitude apart (~60 μs for $MAPbBr_3$ *vs* ~300 μs for $MAPbCl_3$).[35, 70] These findings further support our conclusion that MCS produces a homogenous halide mixture.

The XRD patterns (Figure 3c) for all MCS-HG samples confirm that these consist of a single phase that adopts the cubic *Pm*-3*m* perovskite structure, with diffraction peak positions shifting to higher 2θ values with increasing Cl content.[82] Substituting the chlorine anion (r = 167 pm) with a larger bromine anion (r = 182 pm) increases the lattice parameter, linearly obeying Vegard's law describing solid solution behavior, as shown in Figure 3d.[83] The MCS-HG synthesis method shows a single cutoff energy in the DR spectra (Figure S6), which corresponds systematically to an increase in the bandgap energy from pure $MAPbBr_3$ to pure $MAPbCl_3$ (Figure 3d).

Table 1: Assignment of ^{207}Pb NMR peak positions (δ_{cs}, ppm) for parent and MCS-HG mixed-halide perovskites.[a]

Samples	$[PbBr_6]^{4-}$	$[PbClBr_5]^{4-}$	$[PbCl_2Br_4]^{4-}$	$[PbCl_3Br_3]^{4-}$	$[PbCl_4Br_2]^{4-}$	$[PbCl_5Br]^{4-}$	$[PbCl_6]^{4-}$
$MAPbBr_3$	355						
$MAPb(Cl_{0.05}Br_{0.95})_3$	340 360[b]	175 225[b]					
$MAPb(Cl_{0.25}Br_{0.75})_3$	321	149	-38	−116	−266		
$MAPb(Cl_{0.50}Br_{0.50})_3$	309	119	43	−114	−326	−480	−587
$MAPb(Cl_{0.75}Br_{0.25})_3$		142	53	−160	−360	−500	−622
$MAPb(Cl_{0.83}Br_{0.17})_3$				−174	−368	−520	−627
$MAPb(Cl_{0.95}Br_{0.05})_3$						−400 −450[c]	−641 −621[c]
$MAPbCl_3$							−646
δ_{cs} (ppm)	**332 (30)**	**134 (40)**	**8 (45)**	**−144 (30)**	**−317 (50)**	**−473 (50)**	**−616 (30)**

a. Uncertainties in peak positions range from 5 to 40 ppm, unless noted data is for non-spinning spectra at 11.7 T
b. Determined from a deconvolution of an NMR spectrum obtained under MAS conditions at 7.05 T
c. δ_{iso} determined from ^{207}Pb MAS NMR spectroscopy

A series of DFT calculations on model $[PbX_xX'_{6-x}]^{4-}$ anions (ADF) and periodic solid (CASTEP) models was performed to assess the sensitivity of the ^{207}Pb chemical shift to halide substitution; results are presented in Tables S2 and S4. As shown in Figure 4a, the calculated shielding values for the model anions correlate with the experimentally determined chemical

shifts. The calculated isotropic chemical shifts also reveal a linear relationship, increasing systematically as Cl anions are replaced by Br anions from $[PbCl_6]^{4-}$ to $[PbBr_6]^{4-}$ (Figure 4b). The calculated $\delta_{iso}(^{207}Pb)$ values obtained using the model anions are shown for comparison in Figure 3b, revealing a linear trend to lower chemical shift as Cl is substituted for Br, consistent with our qualitative (experimental $\delta_{cs}(^{207}Pb)$ NMR) assignments of distinct local Pb octahedra found in MHP solid solutions discussed above. Further expanding the model anions to include $MAPbI_3$ and Br/I MHP reveals excellent agreement between the calculated and experimentally determined (*vide infra*) $\delta_{cs}(^{207}Pb)$, demonstrating that the combination of calculated and experimental NMR parameters can be used to assign the distinct short-range order for six-coordinate (i.e., $[PbX_xX'_{6-x}]^{4-}$) chemical environments (Figure 4c). This confirms the qualitative nature of the NMR method in assessing the atomic structure of these single-phase solid-solution materials, which is not obtainable using other traditional analytical methods. We note that the same overall trend is seen for the periodic structure models computed using the GIPAW method within CASTEP, however, the range of calculated shielding values appear to be double those computed with ADF or determined experimentally (Tables S2, S4 and Figure S7). A possible cause for this is the neglect of relativistic effects on the Pb in the CASTEP calculations; better agreement may be achieved by further optimization of the Pb pseudopotential but this is beyond the scope of the work presented here.

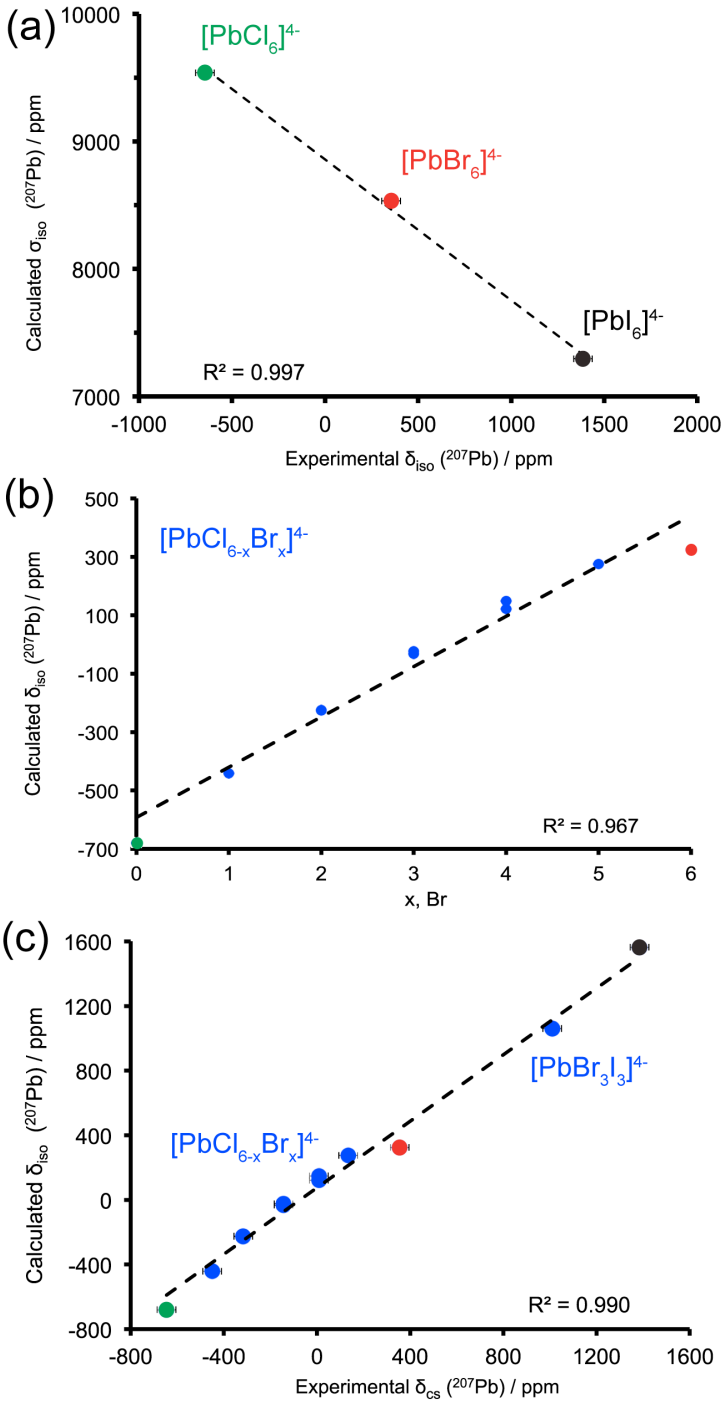

Figure 4: Anion model quantum chemical calculations (ADF) of $[PbX_xX'_{6-x}]^{4-}$ octahedra: calculated shielding vs experimental isotropic chemical shift for the parent perovskites, $MAPbX_3$, where X = Cl, Br or I (a); calculated isotropic chemical shift with Br substitution for Cl anions (b, Calc. $\delta_{iso}(^{207}Pb/ppm) = 172.25x - 592.57$, where x = number of Br neighbors) and relation between calculated isotropic chemical shift and experimental chemical shift of parent compounds $MAPbX_3$, X= Cl, Br and I and their respective MHP (Cl/Br or Br/I) (c, Calc. $\delta_{iso}(^{207}Pb/ppm) = 1.03(Expt.\ \delta_{cs}(^{207}Pb/ppm)) + 75.3$).

The results summarized in Figure 3 are those for a material with very fluid properties whose chemical structure can readily be adapted to randomly accommodate any mixture of halide anions using an MCS method. The diffraction peaks are sharp and of high quality and the one-dimensional ^{207}Pb NMR spectra suggest a binomial-like distribution of Pb sites based on the observed δ_{CS} whose assignment and CSA were estimated through the assistance of DFT calculations (Figure S3). A systematic shift in the bandgap as halide substitution occurs supports the conclusion that these materials exhibit solid-solution behavior, readily adjusting their local ($[PbX_xX'_{6-x}]^{4-}$) and long-range (lattice constant) structure as Cl is replaced by Br. To ascertain that these materials are neither phase-separated nor located within micro/nano scale domains, we investigated these materials using a two-dimensional exchange NMR spectroscopy method.

Figure 5 shows a series of ^{207}Pb 2D EXSY NMR spectra obtained for MCS-synthesized sample $MAPb(Cl_{0.5}Br_{0.5})_3$, acquired with mixing times of 10 and 50 μs, and of 2 ms, compared with those for the parent compounds, $MAPbCl_3$ and $MAPbBr_3$. The spectra for the parent samples obtained with a 10 μs mixing time consist of oval-shaped peaks aligned with the diagonal; with increased mixing time, the peak for $MAPbBr_3$ becomes circular and that for $MAPbCl_3$ broadens. These observations indicate that self-exchange is occurring for both parent compounds and that the rate of exchange is greater for $MAPbBr_3$. In contrast to the spectra for the parent compounds, that for $MAPb(Cl_{0.5}Br_{0.5})_3$ acquired with the shortest mixing time of 10 μs already displays signs of exchange for the individual sites denoted 5, 4 and 3 (i.e., $[PbCl_2Br_4]^{4-}$, $[PbCl_3Br_3]^{4-}$ and $[PbCl_4Br_2]^{4-}$, respectively); increasing the mixing time to 50 μs led to a significant increase in the intensity of the cross peaks. The spectrum obtained with a 2 ms mixing time reveals extensive exchange with cross-peaks amongst the seven distinct $[PbX_xX'_{6-x}]^{4-}$ chemical environments detected. The observation of exchange for the latter sample confirms that

the sample is a solid solution, since neither phase-separated materials nor micro/nano domains would yield EXSY spectra susceptible to fast exchange between the NMR sites attributed to various $[PbX_xX'_{6-x}]^{4-}$ units. The response to the magnitude of the mixing time in the 2D EXSY[46] experiment is an indication of the exchange process, which are typically either a chemical exchange process or a spin diffusion process (i.e., by the direct ^{207}Pb-^{207}Pb dipolar interaction, R_{DD}, for the samples considered here). R_{DD} scales as the inverse cube of the internuclear separation between the coupled nuclei,[84] and thus, based on the crystal structures for the parent compounds, is expected to be on the order of 25 Hz; relatively long mixing times would be required to see cross peaks in 2D EXSY spectra induced by spin exchange. In addition, less than 5 % of the ^{207}Pb nuclei form ^{207}Pb-^{207}Pb spin pairs and thus the EXSY experiment is expected to be relatively insensitive to exchange induced by spin diffusion. Hence the spectra illustrated here are an indication primarily of a halide chemical exchange process. Note that regardless of exchange process, correlations are only expected for a domain-free solid-solution material.

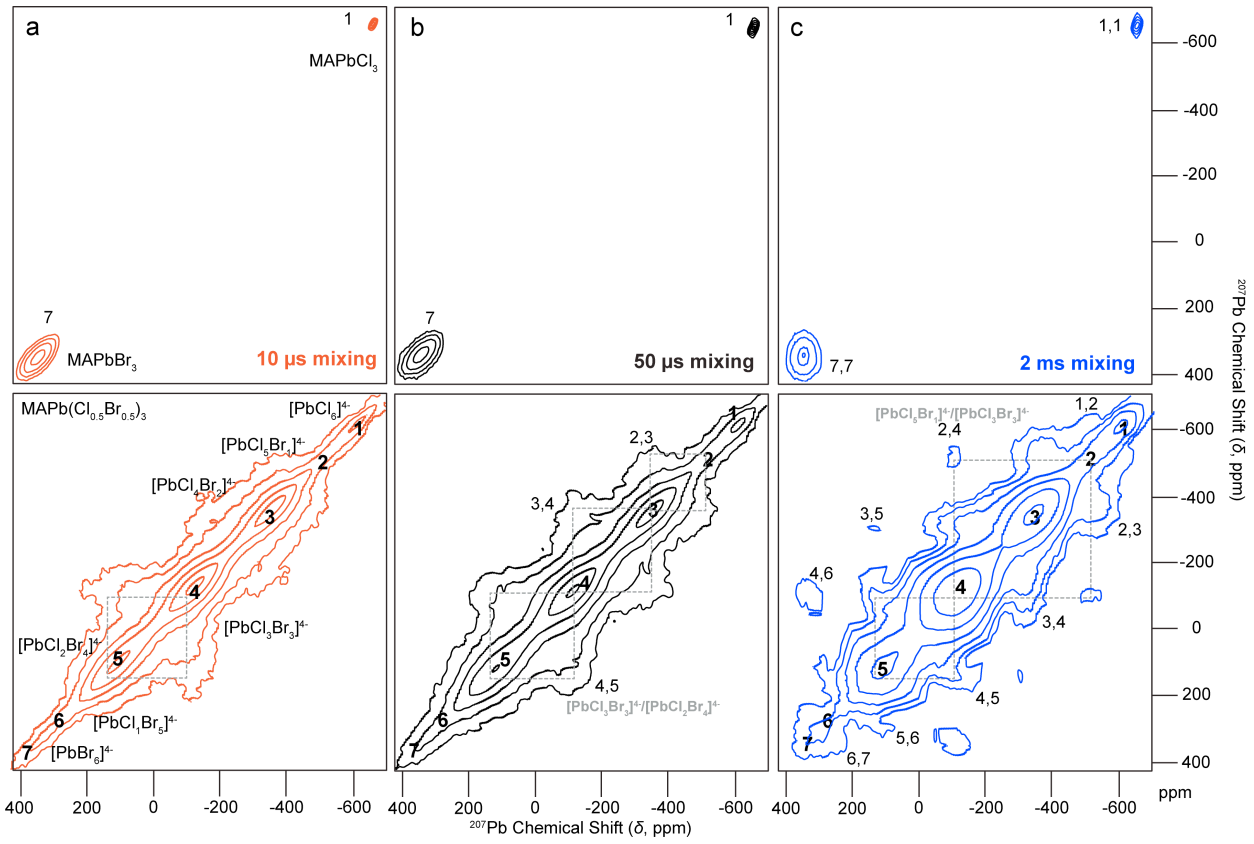

Figure 5: Two-dimensional ^{207}Pb EXSY NMR spectra of $MAPbCl_3$, $MAPbBr_3$ and MCS-HG $MAPb(Cl_{0.5}Br_{0.5})_3$ obtained using 10 µs (a, red), 50 µs (b, black) or 2 ms (c, blue) mixing times. Spectra were acquired at 21.1 T under non-spinning conditions at ambient temperature. Note that the upper spectra are each a superposition of two separate spectra, one for $MAPbCl_3$ and one for $MAPbBr_3$.

Careful analysis of multiple-field NMR spectra (Figure 1), as well as XRD, energy dispersive X-ray (EDX) and DR data, indicate that both the MCS-HG and SS methods create a pure, single-phase crystalline solid. The relative populations of $[PbCl_xBr_{6-x}]^{4-}$ chemical environments obtained using these methods, while somewhat different, behave similarly as the halide distribution changes from Br- to Cl-rich species. Closer examination of the Cl/Br concentrations in the SS sample as determined by EDX reveals that the targeted $MAPb(Cl_{0.5}Br_{0.5})_3$ composition is in fact $MAPb(Cl_{0.58}Br_{0.42})_3$. The non-stoichiometric product obtained with the SS approach is nevertheless consistent with a binomial-like distribution once accounting for the new composition, with the expected chlorine-rich lead octahedra (i.e.,

$[PbCl_6]^{4-}$, $[PbCl_5Br_1]^{4-}$, $[PbCl_4Br_2]^{4-}$ and $[PbCl_3Br_3]^{4-}$) chemical environments (see Figures 1b and 1c and Table S5) over other halide mixing combinations as determined from an analysis of the NMR spectra. Likewise, the sample prepared by the SS method follows Vegard's law, with the lattice constants correlating to the final stoichiometry (see Figure S8 for the XRD pattern of this MHP prepared using the SS method). As for the sample prepared by MCS, there is no indication of phase-separated domains or amorphous structure in the experimental data. In a two-component mixture of $MAPbCl_3$ and $MAPbBr_3$ subjected to MCS, the thermodynamics are different from those in the three-component mixture resulting from SS (i.e., $MAPbCl_3$, $MAPbBr_3$ and the solvent). The former yields a stoichiometric final product while the latter yields a Cl-rich final product due to the altered driving forces for SS (i.e., nucleation and growth) compared to the high-energy MCS method.[85-87]

$MAPb(Cl_xBr_{1-x})_3$ Ball Milling Mechanochemical Synthesis

Figure 6 shows powder XRD and non-spinning NMR spectra, as well as Tauc plots for the $(MAPb(Cl_{0.5}Br_{0.5})_3$ sample prepared using solvent synthesis (SS), hand grinding (MCS-HG) and ball milling (MCS-BM), illustrating the impact of these synthetic approaches on structural and physical properties. Powder XRD data for the samples indicate that the same crystal structure is obtained in all three cases, but the diffraction linewidths indicate that the MCS-BM method yields products that produce broader lines (Figure 6a). The SS and HG samples indicate random distributions of halide environments about the octahedral Pb position $[PbCl_xBr_{6-x}]^{4-}$, with the resonance centered at −100 ppm being attributed to the $[PbCl_3Br_3]^{4-}$ chemical environment, *vide supra*. At low magnetic fields the ^{207}Pb NMR spectrum of the BM sample is featureless (Figures 1, 6b and S9), appearing Gaussian-like in shape, with evidence of multiple Pb octahedral environments only emerging from higher-field ^{207}Pb NMR data (21.1 T, Figure 1a). As for the

SS and HG samples, the solid-solution behavior is preserved for the BM samples. However, the high-energy milling process introduces short-range structural disorder in the otherwise well-ordered cubic environment. This creates a distribution of Pb-X distances and angles, and thus leads to local disorder at the Pb sites, as is evident from the observed linewidths that indicate a distribution of ^{207}Pb chemical shifts, while XRD data indicates that long-range periodic crystallinity is maintained (Figure 6a). The increase in linewidth of the powder XRD pattern and the amorphisation of the well-defined microscopic crystalline solids as observed in field emission scanning electron microscopy, FESEM (Figures S10 and S11), as well as the impact on the MA cation as indicated by ^{1}H and ^{13}C MAS NMR spectroscopy (Figures S12 and S13, respectively) further support the conclusion of local structural disorder determined from the ^{207}Pb NMR spectra.

To examine how the local disorder evolved over time, we obtained ^{207}Pb NMR spectra of samples of $MAPb(Cl_{0.75}Br_{0.25})_3$ prepared with five minutes and with one hour of BM (Figure S14); these spectra confirm that the halide ions quickly begin to mix, already forming a highly ordered random solid solution after five minutes of BM. After one hour of further high-energy milling, a degradation of the local octahedral structure occurs and the $[PbCl_xBr_{6-x}]^{4-}$ octahedra exhibit short-range local disorder (NMR data) within an otherwise preserved hierarchical periodic crystalline solid framework (XRD data).

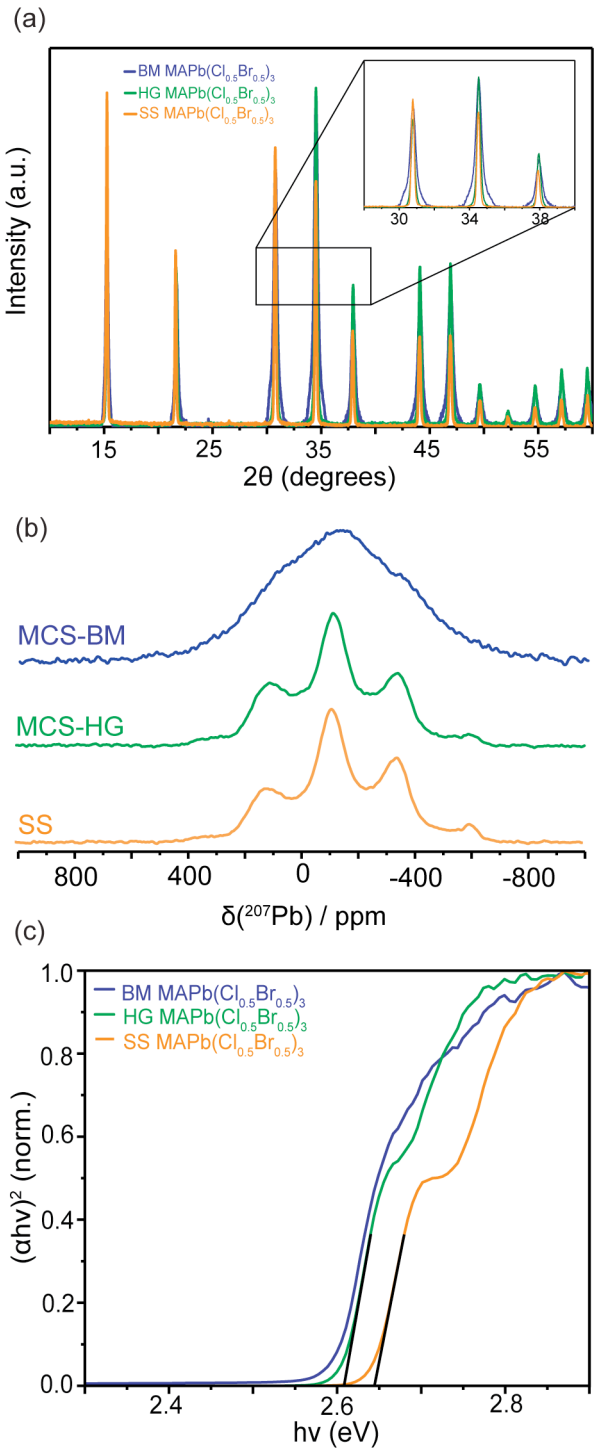

Figure 6: Comparison of data for the $MAPb(Cl_{0.5}Br_{0.5})_3$ MHP prepared using three distinct synthetic approaches: solvent synthesis and mechanochemical synthesis via hand grinding or ball milling. Powder XRD diffraction patterns (a), non-spinning ^{207}Pb NMR spectra, B_0 = 21,1 T (b) and Tauc plots (c). The straight black lines indicate the bandgap energies at the intersection with the abscissa.

The impact of these synthetic approaches and corresponding structural changes on their optical responses were analyzed using DR[88] data (Figure S15); these results indicate similar optical bandgaps for all three $MAPb(Cl_{0.5}Br_{0.5})_3$ samples, but preparing the MHP via the MCS route reduces the bandgap energy by 0.039 eV when compared to the SS technique (2.605 eV for HG vs. 2.644 eV for SS). This change is attributed to the fact that the stoichiometry is preserved when using the MCS approach, as determined by the EDX analysis (Table S5) which indicates that a 1.04:1.0 Cl:Br ratio is obtained for the HG samples (1.09:1 Cl:Br for MCS-BM) while a 1.39:1.0 Cl:Br ratio (i.e., a chlorine-rich solid solution) is obtained for the SS sample, despite the 1:1 synthetic molar ratio of the starting reagents for the preparation of both samples. The MCS approach clearly provides superior ease and control of the composition of the solid solution compared to the SS approach, where the final solid product is driven thermodynamically, requiring one to adjust reactant concentrations in order to achieve a 1:1 synthetic molar ratio. Hence, these results demonstrate that this new solvent-free approach allows one to obtain a homogeneous solid solution using low- (HG) or high-energy (BM) mechanical force chemical synthesis.

MAPb(Br_xI_{1-x})$_3$ Mechanochemical Synthesis

To further investigate the application of the MCS synthetic approach, a 1:1 molar mixture of $MAPbBr_3$ and $MAPbI_3$ was prepared. To determine if the transition from phase-separated parent compounds to a randomly mixed solid solution can be visualized, a sample that was manually hand ground over a period of two hours was characterized by NMR spectroscopy and by XRD, after 1 hr and 2 hrs of hand grinding (Figure 7). The halide ions begin to exchange, immediately forming a solid solution, and after 1 hr of hand grinding, the sample is almost randomly mixed, although XRD and NMR data indicate some of the parent compounds also remain. HG for an additional hour completes the random ordering of the local $[PbBr_xI_{6-x}]^{4-}$ octahedra improving the quality of the solid solution as seen by the narrow diffraction peaks in the XRD data and by a Gaussian-like resonance in the NMR spectrum. The results indicate that the lower energy MCS-HG approach is effective in creating a single-phase MHP, with a binomial-like distribution similar to that obtained from a sample prepared by high-temperature solid-state synthesis.[35] Contrary to the case for the Cl/Br MHP system, we were unable to resolve multiple resonances for the Br/I system in the corresponding ^{207}Pb NMR spectra, although spectra of the parent compounds indicate that substituting I with Br has the same effect as substituting Br with Cl: a shift to lower frequency. The low resolution is primarily attributed to the Pb-I *J*-couplings ($[PbBr_xI_{6-x}]^{4-}$) and the much shorter spin-spin relaxation such that the FWHM for $MAPbI_3$ is ~ 26 kHz,[35, 49, 51, 72] with further complications arising from the various octahedral arrangements and their respective isomers, as discussed above for the Cl/Br solid solutions.

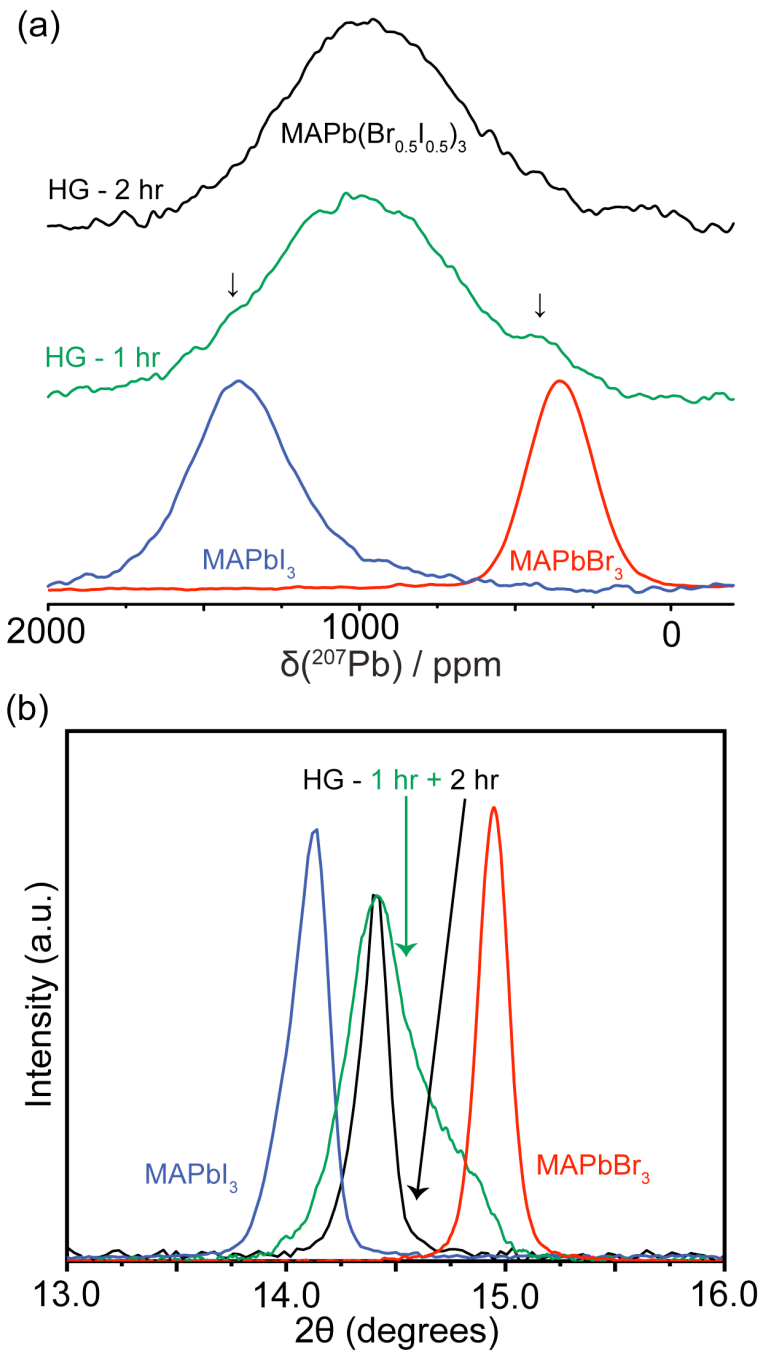

Figure 7: Non-spinning ^{207}Pb NMR (a, 7.05 T) and powder X-ray diffraction spectra (b) for $MAPbBr_3$ (red), $MAPbI_3$ (blue) and $MAPb(Br_{0.5}I_{0.5})_3$ (green 1 hr, black 2 hrs). The MHP samples were prepared by the MCS-HG method for one and two hours. The black arrows in the NMR spectra (a) indicate incomplete random halide mixing after 1 hour (green trace), with small remnants of the parent compounds according to the NMR and XRD data (b, green arrow, 1 hr). The black arrow in (b) indicates complete mixing of a single phase solid solution after 2 hours.

Figures S16 and S17 show the powder XRD and DR data for the parent compounds and the final 50/50 Br/I MHP solid solution prepared by the MCS-HG technique. These data illustrate the benefit of side-stepping the thermodynamically driven solution process (i.e., avoiding the Br-rich phase)[35] with a stoichiometric MCS approach that yields an equal Br/I halide composition, based on XRD and $\delta_{cs}(^{207}Pb)$ data analysis.

CONCLUSIONS

This work demonstrates the utility of the mechanochemical synthetic approach for the preparation of randomly ordered halides in single crystalline MHP solid solutions with enhanced stoichiometric control compared to that achieved using traditional solvent synthetic protocols for the Br/Cl MHPs. Increasing the grinding time and introducing a high-energy milling process maintains the long-range crystalline structure, but it can create a highly disordered local $[PbX_xX'_{6-x}]^{4-}$ octahedral environment due to rearrangements of bond lengths and angles about the Pb center. Carefully tuning the compositions using the MCS-HG method, monitored by one- and two-dimensional ^{207}Pb NMR spectroscopy and supported by quantum chemical calculations, we identified seven distinct Pb octahedral chemical environments in the Br/Cl MHPs, and demonstrated that the synthetic approach can be extended to other Pb-containing mixed halide perovskites. The ^{207}Pb NMR spectra as well as the XRD results for the Cl/Br MHPs obtained using either solution synthesis or MCS of bulk samples indicate single-phase solid solutions with random halide distributions absent of amorphous or phase segregated domains. A stoichiometric $MAPb(Br_{0.5}I_{0.5})_3$ MHP, which has not been achieved previously using traditional room temperature solvent synthesis, was prepared at room temperature using the MCS-HG technique. While ongoing development of perovskite solar cells will require careful characterization, our study has shown that the combination of both X-ray diffraction and solid-state NMR spectroscopy are vital to properly characterize these intrinsically complex materials.

ASSOCIATED CONTENT

SUPPORTING MATERIAL

^{1}H, ^{13}C and ^{207}Pb NMR spectra with spectral simulations, fitting procedure, X-ray diffraction, diffuse reflection, EDX and FESEM data. This material is available free of charge via the Internet at http://pubs.acs.org.

AUTHOR INFORMATION

§Author Contributions: AK and AMA contributed equally to this work

*Corresponding Author: vladimir.michaelis@ualberta.ca

Notes

The authors declare no competing financial interests.

ACKNOWLEDGMENTS

The Natural Sciences and Engineering Research Council (NSERC) of Canada Discovery Grants Program and the University of Alberta are acknowledged for generous research support (V.K.M.). K.S. acknowledges direct and indirect (equipment) funding support from the National Institute for Nanotechnology (NRC-NINT) and Canada Foundation for Innovation. A.M.A. acknowledges scholarship support from Alberta Innovates Technology Futures (AITF). MH is partially supported by the Government of Alberta Queen Elizabeth II Graduate Scholarship. The ATUMS training program supported by NSERC CREATE is thanked for continued generous financial support. Access to the 21.1 T NMR spectrometer was provided by the National Ultrahigh-Field NMR Facility for Solids (Ottawa, Canada), a national research facility funded by a consortium of Canadian Universities and by an NSERC RTI grant, and supported by the National Research Council of Canada and Bruker BioSpin, and managed by the University of Ottawa (http://nmr900.ca).

REFERENCES

1. Shin, S. S.; Yeom, E. J.; Yang, W. S.; Hur, S.; Kim, M. G.; Im, J.; Seo, J.; Noh, J. H.; Seok, S. I., Colloidally Prepared La-Doped $BaSnO_3$ Electrodes for Efficient, Photostable Perovskite Solar Cells. *Science* **2017,** *356*, 167-171.

2. Hsiao, Y.-C.; Wu, T.; Li, M.; Liu, Q.; Qin, W.; Hu, B., Fundamental Physics Behind High-Efficiency Organo-Metal Halide Perovskite Solar Cells. *J. Mater. Chem. A* **2015,** *3* (30), 15372-15385.

3. Miyata, A.; Mitioglu, A.; Plochocka, P.; Portugall, O.; Wang, J. T.-W.; Stranks, S. D.; Snaith, H. J.; Nicholas, R. J., Direct Measurement of the Exciton Binding Energy and Effective Masses for Charge Carriers in Organic-Inorganic Tri-Halide Perovskites. *Nat. Phys.* **2015,** *11* (7), 582-587.

4. Li, Y.; Yan, W.; Li, Y.; Wang, S.; Wang, W.; Bian, Z.; Xiao, L.; Gong, Q., Direct Observation of Long Electron-Hole Diffusion Distance in $CH_3NH_3PbI_3$ Perovskite Thin Film. *Sci. Rep.* **2015,** *5*, 14485.

5. Stranks, S. D.; Nayak, P. K.; Zhang, W.; Stergiopoulos, T.; Snaith, H. J., Formation of Thin Films of Organic–Inorganic Perovskites for High-Efficiency Solar Cells. *Angew. Chem. Int. Ed.* **2015,** *54* (11), 3240-3248.

6. Wong, A. B.; Lai, M.; Eaton, S. W.; Yu, Y.; Lin, E.; Dou, L.; Fu, A.; Yang, P., Growth and Anion Exchange Conversion of $CH_3NH_3PbX_3$ Nanorod Arrays for Light-Emitting Diodes. *Nano Lett.* **2015,** *15* (8), 5519-5524.

7. Tan, H.; Jain, A.; Voznyy, O.; Lan, X.; García de Arquer, F. P.; Fan, J. Z.; Quintero-Bermudez, R.; Yuan, M.; Zhang, B.; Zhao, Y.*, et al.*, Efficient and Stable Solution-Processed Planar Perovskite Solar Cells via Contact Passivation. *Science* **2017,** *355*, 722-726.

8. Eperon, G. E.; Leijtens, T.; Bush, K. A.; Prasanna, R.; Green, T.; Wang, J. T.-W.; McMeekin, D. P.; Volonakis, G.; Milot, R. L.; May, R.*, et al.*, Perovskite-Perovskite Tandem Photovoltaics with Optimized Bandgaps. *Science* **2016,** *354* (6314), 861-865.

9. Jang, D. M.; Park, K.; Kim, D. H.; Park, J.; Shojaei, F.; Kang, H. S.; Ahn, J.-P.; Lee, J. W.; Song, J. K., Reversible Halide Exchange Reaction of Organometal Trihalide Perovskite Colloidal Nanocrystals for Full-Range Band Gap Tuning. *Nano Lett.* **2015,** *15* (8), 5191-5199.

10. Pellet, N.; Teuscher, J.; Maier, J.; Grätzel, M., Transforming Hybrid Organic Inorganic Perovskites by Rapid Halide Exchange. *Chem. Mater.* **2015,** *27* (6), 2181-2188.

11. Colella, S.; Mosconi, E.; Fedeli, P.; Listorti, A.; Gazza, F.; Orlandi, F.; Ferro, P.; Besagni, T.; Rizzo, A.; Calestani, G.*, et al.*, $MAPbI_{3-x}Cl_x$ Mixed Halide Perovskite for Hybrid Solar Cells: The Role of Chloride as Dopant on the Transport and Structural Properties. *Chem. Mater.* **2013,** *25* (22), 4613-4618.

12. Mosconi, E.; De Angelis, F., Mobile Ions in Organohalide Perovskites: Interplay of Electronic Structure and Dynamics. *ACS Energy Lett.* **2016,** *1* (1), 182-188.

13. Brivio, F.; Caetano, C.; Walsh, A., Thermodynamic Origin of Photoinstability in the $CH_3NH_3Pb(I_{1-x}Br_x)_3$ Hybrid Halide Perovskite Alloy. *J. Phys. Chem. Lett.* **2016,** *7* (6), 1083-1087.

14. Hentz, O.; Zhao, Z.; Gradečak, S., Impacts of Ion Segregation on Local Optical Properties in Mixed Halide Perovskite Films. *Nano Lett.* **2016,** *16* (2), 1485-1490.

15. Hoke, E. T.; Slotcavage, D. J.; Dohner, E. R.; Bowring, A. R.; Karunadasa, H. I.; McGehee, M. D., Reversible Photo-Induced Trap Formation in Mixed-Halide Hybrid Perovskites for Photovoltaics. *Chem. Sci.* **2015,** *6* (1), 613-617.

16. Yoon, S. J.; Draguta, S.; Manser, J. S.; Sharia, O.; Schneider, W. F.; Kuno, M.; Kamat, P. V., Tracking Iodide and Bromide Ion Segregation in Mixed Halide Lead Perovskites During Photoirradiation. *ACS Energy Lett.* **2016,** *1* (1), 290-296.

17. Yoon, S. J.; Kuno, M.; Kamat, P. V., Shift Happens. How Halide Ion Defects Influence Photoinduced Segregation in Mixed Halide Perovskites. *ACS Energy Lett.* **2017,** *2* (7), 1507-1514.

18. Lewiński, J.; Dutkiewicz, M.; Lesiuk, M.; Śliwiński, W.; Zelga, K.; Justyniak, I.; Lipkowski, J., Solid-State Conversion of the Solvated Dimer [{*t*BuZn(μ-O*t*Bu)(thf)}$_2$] into a Long Overlooked Trimeric [{*t*BuZnO*t*Bu}$_3$] Species. *Angew. Chem. Int. Ed.* **2010,** *49* (44), 8266-8269.

19. Prochowicz, D.; Justyniak, I.; Kornowicz, A.; Kaczorowski, T.; Kaszkur, Z.; Lewiński, J., Construction of a Porous Homochiral Coordination Polymer with Two Types of Cu_nI_n Alternating Units Linked by Quinine: A Solvothermal and a Mechanochemical Approach. *Chem. - Eur. J.* **2012,** *18* (24), 7367-7371.

20. Prochowicz, D.; Sokołowski, K.; Justyniak, I.; Kornowicz, A.; Fairen-Jimenez, D.; Friščić, T.; Lewiński, J.; Düren, T.; Hyett, G.; Jones, W.*, et al.*, A Mechanochemical Strategy for IRMOF Assembly Based on Pre-Designed Oxo-Zinc Precursors. *Chem. Commun.* **2015,** *51* (19), 4032-4035.

21. Lee, J.; Shin, H.; Lee, J.; Chung, H.; Zhang, Q.; Saito, F., Mechanochemical Syntheses of Perovskite $KM^{II}F_3$ with Cubic Structure (M=Mg, Ca, Mn, Fe, Co, Ni, and Zn). *Mater. Trans.* **2003,** *44* (7), 1457-1460.

22. Elseman, A. M.; Rashad, M. M.; Hassan, A. M., Easily Attainable, Efficient Solar Cell with Mass Yield of Nanorod Single-Crystalline Organo-Metal Halide Perovskite Based on a Ball Milling Technique. *ACS Sustainable Chem. Eng.* **2016,** *4* (9), 4875-4886.

23. Jana, A.; Mittal, M.; Singla, A.; Sapra, S.; Grätzel, M.; Lewiński, J.; Tong, Y.; Polavarapu, L.; Feldmann, J.; Urban, A. S.*, et al.*, Solvent-Free, Mechanochemical Syntheses of Bulk Trihalide Perovskites and Their Nanoparticles. *Chem. Commun.* **2017,** *53* (21), 3046-3049.

24. Zhu, Z.-Y.; Yang, Q.-Q.; Gao, L.-F.; Zhang, L.; Shi, A.-Y.; Sun, C.-L.; Wang, Q.; Zhang, H.-L., Solvent-Free Mechanosynthesis of Composition-Tunable Cesium Lead Halide Perovskite Quantum Dots. *J. Phys. Chem. Lett.* **2017,** *8* (7), 1610-1614.

25. Manukyan, K. V.; Yeghishyan, A. V.; Moskovskikh, D. O.; Kapaldo, J.; Mintairov, A.; Mukasyan, A. S., Mechanochemical Synthesis of Methylammonium Lead Iodide Perovskite. *J. Mater. Sci.* **2016,** *51* (19), 9123-9130.

26. Jodlowski, A. D.; Yépez, A.; Luque, R.; Camacho, L.; de Miguel, G., Benign-by-Design Solventless Mechanochemical Synthesis of Three-, Two-, and One-Dimensional Hybrid Perovskites. *Angew. Chem. Int. Ed.* **2016,** *55* (48), 14972-14977.

27. Prochowicz, D.; Franckevičius, M.; Cieślak, A. M.; Zakeeruddin, S. M.; Grätzel, M.; Lewiński, J., Mechanosynthesis of the Hybrid Perovskite $CH_3NH_3PbI_3$: Characterization and the Corresponding Solar Cell Efficiency. *J. Mater. Chem. A* **2015,** *3* (41), 20772-20777.

28. Prochowicz, D.; Yadav, P.; Saliba, M.; Saski, M.; Zakeeruddin, S. M.; Lewiński, J.; Grätzel, M., Mechanosynthesis of Pure Phase Mixed-Cation $MA_xFA_{1-x}PbI_3$ Hybrid Perovskites: Photovoltaic Performance and Electrochemical Properties. *Sustainable Energy Fuels* **2017,** *1* (4), 689-693.

29. Prochowicz, D.; Yadav, P.; Saliba, M.; Saski, M.; Zakeeruddin, S. M.; Lewiński, J.; Grätzel, M., Reduction in the Interfacial Trap Density of Mechanochemically Synthesized $MAPbI_3$. *ACS Appl. Mater. Interfaces* **2017,** *9* (34), 28418-28425.

30. Kubicki, D.; Prochowicz, D.; Hofstetter, A.; Zakeeruddin, S. M.; Grätzel, M.; Emsley, L., Phase Segregation in Cs-, Rb- and K-Doped Mixed-Cation $(MA)_x(FA)_{1-x}PbI_3$ Hybrid Perovskites from Solid-State NMR. *J. Am. Chem. Soc.* **2017,** *139* (40), 14173-14180.

31. Hibble, S. J.; Chippindale, A. M.; Marelli, E.; Kroeker, S.; Michaelis, V. K.; Greer, B. J.; Aguiar, P. M.; Bilbé, E. J.; Barney, E. R.; Hannon, A. C., Local and Average Structure in Zinc Cyanide: Toward an Understanding of the Atomistic Origin of Negative Thermal Expansion. *J. Am. Chem. Soc.* **2013,** *135* (44), 16478-16489.

32. Aharen, T.; Greedan, J. E.; Ning, F.; Imai, T.; Michaelis, V.; Kroeker, S.; Zhou, H.; Wiebe, C. R.; Cranswick, L. M. D., Magnetic Properties of the *S*=3/2 Geometrically Frustrated Double Perovskites La_2LiRuO_6 and Ba_2YRuO_6. *Phys. Rev. B* **2009,** *80* (13), 134423.

33. Michaelis, V. K.; Greer, B. J.; Aharen, T.; Greedan, J. E.; Kroeker, S., Determining Electron Spin-Transfer Mechanisms in Paramagnetic Ba_2YMO_6 (M = Mo, Re, Ru) Double Perovskites by ^{89}Y and ^{137}Ba MAS NMR Spectroscopy. *J. Phys. Chem. C* **2012,** *116* (44), 23646-23652.

34. Grey, C. P.; Smith, M. E.; Cheetham, A. K.; Dobson, C. M.; Dupree, R., Yttrium-89 Magic Angle Spinning NMR Study of Rare-Earth Pyrochlores: Paramagnetic Shifts in the Solid State. *J. Am. Chem. Soc.* **1990,** *112* (12), 4670-4675.

35. Rosales, B. A.; Men, L.; Cady, S. D.; Hanrahan, M. P.; Rossini, A. J.; Vela, J., Persistent Dopants and Phase Segregation in Organolead Mixed-Halide Perovskites. *Chem. Mater.* **2016,** *28* (19), 6848-6859.

36. Maculan, G.; Sheikh, A. D.; Abdelhady, A. L.; Saidaminov, M. I.; Haque, M. A.; Murali, B.; Alarousu, E.; Mohammed, O. F.; Wu, T.; Bakr, O. M., $CH_3NH_3PbCl_3$ Single Crystals: Inverse

Temperature Crystallization and Visible-Blind UV-Photodetector. *J. Phys. Chem. Lett.* **2015,** *6* (19), 3781-3786.

37. Saidaminov, M. I.; Abdelhady, A. L.; Murali, B.; Alarousu, E.; Burlakov, V. M.; Peng, W.; Dursun, I.; Wang, L.; He, Y.; Maculan, G.*, et al.*, High-Quality Bulk Hybrid Perovskite Single Crystals within Minutes by Inverse Temperature Crystallization. *Nat. Commun.* **2015,** *6*, 7586.

38. Pines, A.; Gibby, M. G.; Waugh, J. S., Proton-Enhanced Nuclear Induction Spectroscopy. A Method for High Resolution NMR of Dilute Spins in Solids. *J. Chem. Phys.* **1972,** *56* (4), 1776-1777.

39. Earl, W. L.; Vanderhart, D. L., Measurement of ^{13}C Chemical Shifts in Solids. *J. Magn. Reson. (1969)* **1982,** *48* (1), 35-54.

40. Bennett, A. E.; Rienstra, C. M.; Auger, M.; Lakshmi, K. V.; Griffin, R. G., Heteronuclear Decoupling in Rotating Solids. *J. Chem. Phys.* **1995,** *103* (16), 6951-6958.

41. Hahn, E. L., Spin Echoes. *Phys. Rev.* **1950,** *80*, 580.

42. Mansfield, P., Multiple-Pulse Nuclear Magnetic Resonance Transients in Solids. *Phys. Rev.* **1965,** *137* (3A), A961-A974.

43. Bodart, P. R.; Amoureux, J.-P.; Dumazy, Y.; Lefort, R., Theoretical and Experimental Study of Quadrupolar Echoes for Half-Integer Spins in Static Solid-State NMR. *Mol. Phys.* **2000,** *98* (19), 1545-1551.

44. Davis, J. H.; Jeffrey, K. R.; Bloom, M.; Valic, M. I.; Higgs, T. P., Quadrupolar Echo Deuteron Magnetic Resonance Spectroscopy in Ordered Hydrocarbon Chains. *Chem. Phys. Lett.* **1976,** *42* (2), 390-394.

45. Massiot, D.; Farnan, I.; Gautier, N.; Trumeau, D.; Trokiner, A.; Coutures, J. P., ^{71}Ga and ^{69}Ga Nuclear Magnetic Resonance Study of B-Ga_2O_3: Resolution of Four- and Six-Fold Coordinated Ga Sites in Static Conditions. *Solid State Nucl. Magn. Reson.* **1995,** *4* (4), 241-248.

46. Jeener, J.; Meier, B. H.; Bachmann, P.; Ernst, R. R., Investigation of Exchange Processes by Two-Dimensional NMR Spectroscopy. *J. Chem. Phys.* **1979,** *71* (11), 4546-4553.

47. Bernard, G. M.; Goyal, A.; Miskolzie, M.; McKay, R.; Wu, Q.; Wasylishen, R. E.; Michaelis, V. K., Methylammonium Lead Chloride: A Sensitive Sample for an Accurate NMR Thermometer. *J. Magn. Reson.* **2017,** *283* (Supplement C), 14-21.

48. Eichele, K. *Wsolids NMR Simulation Package*, 1.20.21; Universität Tübingen, 2013.

49. Askar, A. M.; Bernard, G. M.; Wiltshire, B.; Shankar, K.; Michaelis, V. K., Multinuclear Magnetic Resonance Tracking of Hydro, Thermal, and Hydrothermal Decomposition of $CH_3NH_3PbI_3$. *J. Phys. Chem. C* **2017,** *121* (2), 1013-1024.

50. Rosales, B. A.; Hanrahan, M. P.; Boote, B. W.; Rossini, A. J.; Smith, E. A.; Vela, J., Lead Halide Perovskites: Challenges and Opportunities in Advanced Synthesis and Spectroscopy. *ACS Energy Lett.* **2017,** *2* (4), 906-914.

51. Senocrate, A.; Moudrakovski, I.; Kim, G. Y.; Yang, T.-Y.; Gregori, G.; Grätzel, M.; Maier, J., The Nature of Ion Conduction in Methylammonium Lead Iodide: A Multimethod Approach. *Angew. Chem. Int. Ed.* **2017,** *56* (27), 7755-7759.

52. Dybowski, C.; Smith, M. L.; Hepp, M. A.; Gaffney, E. J.; Neue, G.; Perry, D. L., ^{207}Pb NMR Chemical-Shift Tensors of the Lead (II) Halides and the Lead (II) Hydroxyhalides. *Appl. Spectrosc.* **1998,** *52* (3), 426-429.

53. Taylor, R. E.; Beckmann, P. A.; Bai, S.; Dybowski, C., ^{127}I and ^{207}Pb Solid-State NMR Spectroscopy and Nuclear Spin Relaxation in PbI_2: A Preliminary Study. *J. Phys. Chem. C* **2014,** *118* (17), 9143-9153.

54. ADF2017, SCM; Theoretical Chemistry, Vrije Universiteit, Amsterdam, The Netherlands, http://www.scm.com.

55. Fonseca Guerra, C.; Snijders, J. G.; Te Velde, G.; Baerends, E. J., Towards an Order-N DFT Method. *Theor. Chem. Acc.* **1998,** *99* (6), 391-403.

56. Te Velde, G.; Bickelhaupt, F. M.; Baerends, E. J.; Fonseca Guerra, C.; van Gisbergen, S. J. A.; Snijders, J. G.; Ziegler, T., Chemistry with ADF. *J. Comput. Chem.* **2001,** *22* (9), 931-967.

57. Jaffe, A.; Lin, Y.; Beavers, C. M.; Voss, J.; Mao, W. L.; Karunadasa, H. I., High-Pressure Single-Crystal Structures of 3D Lead-Halide Hybrid Perovskites and Pressure Effects on Their Electronic and Optical Properties. *ACS Cent. Sci.* **2016,** *2* (4), 201-209.

58. Lenthe, E. V.; Ehlers, A.; Baerends, E.-J., Geometry Optimizations in the Zero Order Regular Approximation for Relativistic Effects. *J. Chem. Phys.* **1999,** *110* (18), 8943-8953.

59. Schreckenbach, G.; Ziegler, T., Calculation of NMR Shielding Tensors Using Gauge-Including Atomic Orbitals and Modern Density Functional Theory. *J. Phys. Chem.* **1995,** *99* (2), 606-611.

60. Mason, J., Conventions for the Reporting of Nuclear Magnetic Shielding (or Shift) Tensors Suggested by Participants in the Nato Arw on NMR Shielding Constants at the University of Maryland, College Park, July 1992. *Solid State Nucl. Magn. Reson.* **1993,** *2* (5), 285-288.

61. Herzfeld, J.; Berger, A. E., Sideband Intensitites in NMR-Spectra of Samples Spinning at the Magic Angle. *J. Chem. Phys.* **1980,** *73* (12), 6021-6030.

62. Perdew, J. P.; Burke, K.; Ernzerhof, M., Generalized Gradient Approximation Made Simple. *Phys. Rev. Lett.* **1996,** *77*, 3865.

63. Perdew, J. P.; Burke, K.; Ernzerhof, M., Perdew, Burke, and Ernzerhof Reply. *Phys. Rev. Lett.* **1998,** *80*, 891.

64. Perdew, J. P.; Burke, K.; Ernzerhof, M., Generalized Gradient Approximation Made Simple [Phys. Rev. Lett. 77, 3865 (1996)]. *Phys. Rev. Lett.* **1997,** *78*, 1396.

65. Clark, S. J.; Segall, M. D.; Pickard, C. J.; Hasnip, P. J.; Probert, M. I. J.; Refson, K.; Payne, M. C., First Principles Methods Using Castep. *Z. Kristallogr. - Cryst. Mater.* **2005,** *220*, 567−570.

66. Yates, J. R.; Pickard, C. J.; Mauri, F., Calculation of NMR Chemical Shifts for Extended Systems Using Ultrasoft Pseudopotentials. *Phys. Rev. B* **2007,** *76*, 024401.

67. Baikie, T.; Barrow, N. S.; Fang, Y.; Keenan, P. J.; Slater, P. R.; Piltz, R. O.; Gutmann, M.; Mhaisalkar, S. G.; White, T. J., A Combined Single Crystal Neutron/X-Ray Diffraction and Solid-State Nuclear Magnetic Resonance Study of the Hybrid Perovskites $CH_3NH_3PbX_3$ (X = I, Br and Cl). *J. Mater. Chem. A* **2015,** *3* (17), 9298-9307.

68. Misra, R. K.; Ciammaruchi, L.; Aharon, S.; Mogilyansky, D.; Etgar, L.; Visoly-Fisher, I.; Katz, E. A., Effect of Halide Composition on the Photochemical Stability of Perovskite Photovoltaic Materials. *ChemSusChem* **2016,** *9* (18), 2572-2577.

69. Rehman, W.; McMeekin, D. P.; Patel, J. B.; Milot, R. L.; Johnston, M. B.; Snaith, H. J.; Herz, L. M., Photovoltaic Mixed-Cation Lead Mixed-Halide Perovskites: Links between Crystallinity, Photo-Stability and Electronic Properties. *Energy Environ. Sci.* **2017,** *10* (1), 361-369.

70. Roiland, C.; Trippe-Allard, G.; Jemli, K.; Alonso, B.; Ameline, J.-C.; Gautier, R.; Bataille, T.; Le Polles, L.; Deleporte, E.; Even, J.*, et al.*, Multinuclear NMR as a Tool for Studying Local Order and Dynamics in $CH_3NH_3PbX_3$ (X = Cl, Br, I) Hybrid Perovskites. *Phys. Chem. Chem. Phys.* **2016,** *18* (39), 27133-27142.

71. Wasylishen, R. E.; Knop, O.; Macdonald, J. B., Cation Rotation in Methylammonium Lead Halides. *Solid State Commun.* **1985,** *56* (7), 581-582.

72. Bernard, G. M.; Wasylishen, R. E.; Ratcliffe, C. I.; Terskikh, V. V.; Wu, Q.; Buriak, J. M.; Hauger, T., Methylammonium Cation Dynamics in Methylammonium Lead Halide Perovskites–A Solid-State NMR Perspective. *J. Phys. Chem. A* **2018,** *122* (6), 1560-1573.

73. Kubicki, D. J.; Prochowicz, D.; Hofstetter, A.; Péchy, P.; Zakeeruddin, S. M.; Grätzel, M.; Emsley, L., Cation Dynamics in Mixed-Cation $(MA)_x(FA)_{1-x}PbI_3$ Hybrid Perovskites from Solid-State NMR. *J. Am. Chem. Soc.* **2017,** *139* (29), 10055-10061.

74. Franssen, W. M. J.; van Es, S. G. D.; Dervişoğlu, R.; de Wijs, G. A.; Kentgens, A. P. M., Symmetry, Dynamics, and Defects in Methylammonium Lead Halide Perovskites. *J. Phys. Chem. Lett.* **2017,** *8* (1), 61-66.

75. Fayon, F.; Bessada, C.; Massiot, D.; Farnan, I.; Coutures, J. P., ^{29}Si and ^{207}Pb NMR Study of Local Order in Lead Silicate Glasses. *J. Non-Cryst. Solids* **1998,** *232-234* (Supplement C), 403-408.

76. Martin, V.; Wood, B.; Werner-Zwanziger, U.; Zwanziger, J. W., Structural Aspects of the Photoelastic Response in Lead Borate Glasses. *J. Non-Cryst. Solids* **2011,** *357* (10), 2120-2125.

77. Keeler, E. G.; Michaelis, V. K.; Colvin, M. T.; Hung, I.; Gor'kov, P. L.; Cross, T. A.; Gan, Z.; Griffin, R. G., ^{17}O MAS NMR Correlation Spectroscopy at High Magnetic Fields. *J. Am. Chem. Soc.* **2017,** *139* (49), 17953-17963.

78. Xu, Q.; Eguchi, T.; Nakayama, H.; Nakamura, N.; Kishita, M., Molecular Motions and Phase Transitions in Solid $CH_3NH_3PbX_3$ (X = C1, Br, I) as Studied by NMR and NQR. *Z. Naturforsch. A* **1991**; *46* (3), 240-246.

79. Harris, R. K.; Olivieri, A. C., Quadrupolar Effects Transferred to Spin-1/2 Magic-Angle Spinning Spectra of Solids. *Prog. Nucl. Magn. Reson. Spectrosc.* **1992,** *24* (5), 435-456.

80. Wrackmeyer, B., Application of ^{207}Pb NMR Parameters. *Annu. Rep. NMR Spectrosc.* **2002**; *47*, 1-37.

81. Dybowski, C.; Neue, G., Solid State ^{207}Pb NMR Spectroscopy. *Prog. Nucl. Magn. Reson. Spectrosc.* **2002,** *41*, 153-170.

82. Dong, X.; Fang, X.; Lv, M.; Lin, B.; Zhang, S.; Ding, J.; Yuan, N., Improvement of the Humidity Stability of Organic-Inorganic Perovskite Solar Cells Using Ultrathin Al_2O_3 Layers Prepared by Atomic Layer Deposition. *J. Mater. Chem. A* **2015,** *3* (10), 5360-5367.

83. Vegard, L., Die Konstitution Der Mischkristalle Und Die Raumfüllung Der Atome. *Z. Phys.* **1921,** *5* (1), 17-26.

84. Wasylishen, R. E., Indirect Nuclear Spin-Spin Coupling Tensors. *eMagRes*, John Wiley & Sons, Ltd: 2007.

85. Liang, P.-W.; Liao, C.-Y.; Chueh, C.-C.; Zuo, F.; Williams, S. T.; Xin, X.-K.; Lin, J.; Jen, A. K. Y., Additive Enhanced Crystallization of Solution-Processed Perovskite for Highly Efficient Planar-Heterojunction Solar Cells. *Adv. Mater.* **2014,** *26* (22), 3748-3754.

86. Manser, J. S.; Saidaminov, M. I.; Christians, J. A.; Bakr, O. M.; Kamat, P. V., Making and Breaking of Lead Halide Perovskites. *Acc. Chem. Res.* **2016,** *49* (2), 330-338.

87. Tidhar, Y.; Edri, E.; Weissman, H.; Zohar, D.; Hodes, G.; Cahen, D.; Rybtchinski, B.; Kirmayer, S., Crystallization of Methyl Ammonium Lead Halide Perovskites: Implications for Photovoltaic Applications. *J. Am. Chem. Soc.* **2014,** *136* (38), 13249-13256.

88. Tauc, J.; Grigorovici, R.; Vancu, A., Optical Properties and Electronic Structure of Amorphous Germanium. *Phys. Status Solidi B* **1966,** *15* (2), 627-637.

TABLE OF CONTENTS GRAPHIC